










Article

Evaluating PlanetScope and UAV Multispectral Data for Monitoring Winter Wheat and Sustainable Fertilization Practices in Mediterranean Agroecosystems

Italo Moletto-Lobos ¹, Katarzyna Cyran ¹, Luciano Orden ^{2,3}, Silvia Sánchez-Méndez ², Belen Franch ^{1,4,*}, Natacha Kalecinski ⁴, Francisco J. Andreu-Rodríguez ², Miguel Á. Mira-Urios ², José A. Saéz-Tovar ², Pierre C. Guillevic ⁵ and Raul Moral ²

¹ Global Change Unit, Image Processing Laboratory, Universitat de Valencia, 46980 Paterna, Spain; italo.moletto@uv.es (I.M.-L.)

² Instituto de Investigación e Innovación Agrolimentaria y Agroambiental (CIAGRO-UMH), Universidad Miguel Hernández, Carretera de Carretera de Beniel Km 3.2, 03312 Orihuela, Spain

³ Departamento de Agronomía, Universidad Nacional del Sur (UNS), San Andrés 800, Bahía Blanca 8000, Buenos Aires, Argentina

⁴ Department of Geographical Sciences, University of Maryland, College Park, MD 20742, USA

⁵ Planet Labs Germany GmbH, Kurfürstendamm 22, 10719 Berlin, Germany

* Correspondence: belen.franch@uv.es

Abstract: Cereal crops play a critical role in global food security, but their productivity is increasingly threatened by climate change. This study evaluates the feasibility of using PlanetScope satellite imagery and a UAV equipped with the MicaSense RedEdge multispectral imaging sensor in monitoring winter wheat under various fertilizer treatments in a Mediterranean climate. Eleven fertilizer treatments, including organic-mineral fertilizer (OMF) pellets, were tested. The results show that conventional inorganic fertilization provided the highest yield (8618 kg ha⁻¹), while yields from OMF showed a comparable performance to traditional fertilizers, indicating their potential for sustainable agriculture. PlanetScope data demonstrated moderate accuracy in predicting canopy cover ($R^2 = 0.68$), crop yield ($R^2 = 0.54$), and grain quality parameters such as protein content ($R^2 = 0.49$), starch ($R^2 = 0.56$), and hectoliter weight ($R^2 = 0.51$). However, its coarser resolution limited its ability to capture finer treatment-induced variability. MicaSense, despite its higher spatial resolution, performed poorly in predicting crop components, with R^2 values below 0.35 for yield and protein content. This study highlights the complementary use of remote sensing technologies to optimize wheat management and support climate-resilient agriculture through the integration of sustainable fertilization strategies.

Keywords: remote sensing; satellite; UAV; organo-mineral fertilization; extensive crops; vegetation monitoring; phenology; yield prediction



Citation: Moletto-Lobos, I.; Cyran, K.; Orden, L.; Sánchez-Méndez, S.; Franch, B.; Kalecinski, N.; Andreu-Rodríguez, F.J.; Mira-Urios, M.Á.; Saéz-Tovar, J.A.; Guillevic, P.C.; et al. Evaluating PlanetScope and UAV Multispectral Data for Monitoring Winter Wheat and Sustainable Fertilization Practices in Mediterranean Agroecosystems. *Remote Sens.* **2024**, *16*, 4474. <https://doi.org/10.3390/rs16234474>

Academic Editor: Wenjiang Huang

Received: 14 October 2024

Revised: 17 November 2024

Accepted: 25 November 2024

Published: 28 November 2024



Copyright: © 2024 by the authors. Licensee MDPI, Basel, Switzerland. This article is an open access article distributed under the terms and conditions of the Creative Commons Attribution (CC BY) license (<https://creativecommons.org/licenses/by/4.0/>).

1. Introduction

Wheat (*Triticum* spp. L.) is a fundamental component of the global diet, providing essential nutrients and serving as a critical foundation for global food security [1,2]. As a staple food, wheat contributes to the caloric intake of over 35% of the world's population and accounts for approximately 20% of global dietary protein [3]. However, its stability and productivity are increasingly threatened by global warming and a range of extreme climatic events that have led to yield reductions of up to 6% per degree (°C) increase in global temperature [4,5]. These events include frosts, reduced solar radiation, droughts, and heat waves [6–9], which significantly affect crop yields and threaten food security. Monitoring the condition and development of wheat during the growing season is critical for assessing crop quality and making informed management decisions. Key indicators such as phenological metrics, such as the start of the season (SOS), peak of the season (POS), length of the season (LOS), and end of the season (EOS), or other biophysical parameters

such as the fraction of green vegetation cover (fCover), yield prediction, or protein content quantification can provide valuable insights into the wheat status and performance [10–13]. By evaluating these parameters, it is possible to understand how the wheat is progressing, allowing for the selection of optimal treatment and fertilization strategies where necessary. This proactive approach ensures timely and effective interventions, ultimately improving yield and quality.

Fertilizers enable 50% of food production and contribute to food security in the EU. The amount of mineral fertilizers, including nitrogen (N) and phosphorus (P), used in EU agricultural production was 11.2 Mt in 2020 [14]. Agricultural activities generate a quantity of non-productive biomass that can be used for bioenergy production and the fertilization of agricultural soils. The recycling of solid organic waste is currently a priority issue in the EU policy framework. A feasible technique to obtain secondary products from the waste generated is composting, which allows obtaining a stabilized and mature material with fertilizing power, improving the physical, chemical, and biological properties of the soil [15], and providing the soil with a suppressive capacity against certain pathogens as it stimulates the soil microbiota [16].

Regardless of the benefits of compost, it has some limitations for storage and transport due to its low density and the emission of dust and possible inhalation of volatile organic compounds during application [17]. The pelletization process consists of the mechanical compression of the biomass, thus increasing the density of the compost and facilitating both the storage and transport of this biofertilizer, making it a feasible solution to address the problems described above [18]. Therefore, the development of advanced organic fertilizers is necessary, as they contribute to both fertilization and carbon C sequestration in the soil [19,20] and, indirectly, to the reduction of greenhouse gases (GHG) emissions by relying less on energy processes and having a slower nutrient release. These proposed solutions would be in line with the EU's 'Farm to Fork Strategy' of promoting more sustainable agriculture, reducing GHG emissions, and reducing the use of pesticides and chemical fertilizers, with an integrated approach in the circular economy [14]. The generation of organo-mineral pelletized products as alternatives to conventional fertilizers is essential, both to ensure food production and to adapt to climate change.

Remote sensing is a key tool for monitoring wheat crops, providing essential parameters such as fCover, yield prediction using optical signals, and biophysical models [21–24]. It allows for continuous monitoring throughout the growing season, from early to late stages, providing timely information critical for decision making [25–27]. By analyzing remote sensing data, farmers and agricultural managers can make informed decisions about interventions such as irrigation, fertilization, and pest control [28,29]. Several studies have demonstrated the utility of freely and commercially available satellite data for field-scale monitoring. For example, Sentinel-2, with its high-resolution imagery and frequent revisit time, is often used to assess vegetation indices and estimate yield at the field level [30–32]. With a daily revisit and a spatial resolution of 3.7 m, PlanetScope data from Planet SuperDove satellites provide even more detailed insights, making them particularly useful for in-field studies and applications involving smallholder farmers [33,34]. Despite these advances, there remains a gap in the literature regarding the use of PlanetScope data for experimental-scale analysis, even though its daily, high-resolution imagery has significant potential to improve crop management strategies, the monitoring of biophysical variables, and yield prediction. Unmanned aerial vehicles (UAVs) complement these data sources by capturing high-resolution imagery for experimental-scale analyses, allowing the detailed examination of specific plots or experimental setups [35,36]. Further exploration of this area could lead to optimized crop management and improved agricultural outcomes.

Sustainable agriculture increasingly requires innovative tools to monitor crops and optimize management practices. Remote sensing technologies, with their ability to capture detailed phenological and biophysical information, offer valuable insights into crop performance, particularly under varied fertilization regimes. This study hypothesizes that high spatial and temporal resolution remote sensing tools, such as PlanetScope satellite

imagery and UAV-based multispectral data, can effectively monitor key parameters of winter wheat at the parcel scale, while capturing the effects of sustainable fertilization practices under Mediterranean conditions. The main objective is to evaluate the feasibility of using these tools for monitoring small plots of winter wheat under Mediterranean conditions, specifically, determining how PlanetScope's high-resolution imagery can retrieve land surface phenology and key biophysical parameters of the crop. Additionally, the research investigates the prediction of crop yield and protein content using remote sensing data and evaluates the performance of these predictions under different treatments of organic-mineral fertilizer pellets. By leveraging the complementary strengths of these technologies, this study aims to enhance precision and sustainability in crop management practices.

2. Materials and Methods

2.1. Study Area and Experimental Design

The field experiment was carried out during the 2022/2023 winter crop season at a research field of Aula Dei Experimental Station (EEAD-CSIC) in Zaragoza, northeastern Spain ($41^{\circ}44'21.7''N$, 0° the $46'40.5''W$, 255 m altitude), in a semiarid agroecosystem of the Ebro river valley (northeastern Spain) characterized by erratic annual rainfall and high evapotranspiration [37]. The average annual rainfall is 339.2 mm and the mean temperature is $14.6^{\circ}C$. The potential evapotranspiration rate exceeds 1200 mm year^{-1} . The average temperature during the 224-day experimental period was $12.5^{\circ}C$, the total rainfall was 130 mm, and average relative humidity was 72% (18 November 2022–30 June 2023). The meteorological data of this experiment (224 days) were obtained from a meteorological station belonging to the network of the Ministry of Agriculture of the Spanish Government SIAR, located near the experimental site (Table S1). The soil type is loam (fine-loamy, mixed, thermic Xerollic Calciorthid) according to the USDA soil classification [38]. Regarding the characterization of the topsoil layer (0–20 cm), the pH (1:25 *w/v*), electrical conductivity (EC) (1:2.5 soil-water ratio), and organic matter (OM) are 8.43, $236\ \mu\text{S m}^{-1}$, and 1.67%, respectively.

The experimental design was a randomized complete block with three replicates (plot size $8\text{ m} \times 3\text{ m}$) (Figure 1) in the frame assay of Sánchez-Méndez et al. [39]. Eleven fertilizing treatments, including a treatment not fertilized (Control, 00), were tested (Table 1) on wheat (*Triticum turgidum* L. Subsp. durum cv. Sculptur) at a seed rate of 250 kg ha^{-1} and a row spacing of 17.5 cm. P fertilization was applied at sowing on 18th November (day 0), $Z_{0,0}$ [40], normalized to 50 kg P ha^{-1} ; N fertilization, normalized to 150 kg N ha^{-1} , was applied at tillering on 16th February (day 90, $Z_{2,3}$), according to the recommendation for the study area [41]. All fertilizers were applied manually at surface broadcast.

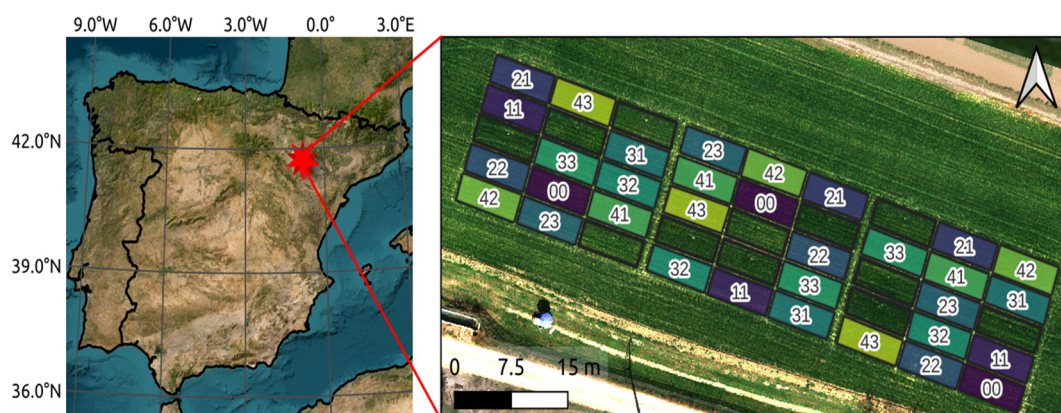


Figure 1. Test site for the 2022–2023 winter wheat campaign: rectangles mark the plot subsets.

Table 1. Mineral fertilizer combinations and fertilization doses of wheat for the trial conducted at Aula Dei Experimental Station (EEAD-CSIC).

Treatment	ID	P Source (Z _{0,0})	N Source (Z _{2,3})
Control	00	--	--
P(MAP) + N(UREA)	11	MAP	Urea
P(MAP + C) + N(UREA)	21	Compost + MAP	Urea
P(MAP + C) + N(UREA + C)	22	Compost + MAP	Compost + Urea
P(MAP + C) + N(BIM + C)	23	Compost + MAP	Compost + Blood meal
P(BM + C) + N(UREA)	31	Compost + Bone meal	Urea
P(BM + C) + N(UREA + C)	32	Compost + Bone meal	Compost + Urea
P(BM + C) + N(BIM + C)	33	Compost + Bone meal	Compost + Blood meal
P(Str+C) + N(UREA)	41	Compost + Struvite	Urea
P(Str + C) + N(UREA + C)	42	Compost + Struvite	Compost + Urea
P(Str + C) + N(BIM + C)	43	Compost + Struvite	Compost + Blood meal

Control: not fertilized. P and N indicate phosphorus and nitrogen, respectively. MAP: monoammonium phosphate (11-61-0); UREA: urea (46-0-0). C: compost; BIM: blood meal; BM: bone meal; Str: struvite.

The source of inorganic P fertilizers was monoammonium phosphate (MAP, 11-61-0) and the source of inorganic N was urea (46-0-0). The organic-mineral fertilizer (OMF) and organic fertilizer (OF) pellets were prepared from compost (olive mill waste–poultry manure–olive leaf waste; 60:20:20) produced by large-scale windrow composting [42], air-dried and mixed with the P and N nutrient sources. For OMF pellets used as P sources, the compost was mixed with MAP (MAP + C) and struvite (Str + C) and for OF pellets used as P sources, the compost was mixed with bone meal (BM + C). For OMF and OF pellets used as N source, the compost was combined with urea (Urea + C) and blood meal (BIM + C), respectively (Table 1). Pellets were produced at CompoLab EPSO-UMH (Orihuela, Spain) by extrusion of the mixtures with a small-scale pelletizer machine (4 HP), reaching a final size of 5 mm in length and 5 mm in diameter. Furrow irrigation was performed on 24 March, 23 April, and 12 May, coinciding with the grain development stage (Z8.7).

The trial was carried out in a conventional tillage system, with lucerne (*Medicago sativa* L.) as the preceding crop and the soil prepared by moldboard plowing. Weeds were chemically controlled (2,4-dichlorophenoxyacetic acid) at recommended rates (1 L ha⁻¹), with all treatments receiving the same level of pest control on 14 March.

2.2. Field Data Acquisition

During the crop season, fraction of vegetation (fCover) was measured with the Canopeo app [43]. The app is based on red-to-green color relations (R/G), blue-to-green colors (B/G), and an excess index of green (2G–R–B). Measurements were conducted at a height of 1.5 m above the ground [44]. In each plot, a sample of 8 m length of each plot (video composite of 20 photographs) was obtained as a percentage cover result.

At physiological maturity (Z_{9,0}), wheat spikes from the 8 m² central rows in each plot were machine-harvested and weighed in the field, standardizing the values at 10% grain moisture (kg ha⁻¹). The mineral composition of the tissues was determined by nitric perchloric acid digestion [45]. The total C and N content of the tissues samples was determined in automatic elemental microanalyzer (EuroVector elemental analyzer, Milan, Italy) and expressed as %N [46]. The total N of the grains was obtained and protein content (PB %) of the grain was determined using a conversion factor of 5.75 [47] and the hectoliter weight (HW %) was measured (kg hL⁻¹).

Statistical analyses were performed using the Infostat v.2020 statistical software package linked to the R programme v3.6.3 [48]. Normality of the data was tested using the Shapiro–Wilks test and the homogeneity of variance was assessed and confirmed using the Levene test ($p > 0.05$).

The analysis of variance (ANOVA test at $p < 0.05$) was performed for all the experimental variables using a generalized linear mixed model, with fertilizer treatments and sampling dates as fixed factors and each plot as a random factor. Multiple comparisons between the means were made using the LSD (least significant difference) Fisher test ($\alpha = 0.05$). This approach tests for significant differences in the means of the experimental variables across fertilizer treatments and sampling dates, using the ANOVA technique as the primary method for evaluating factor-level effects.

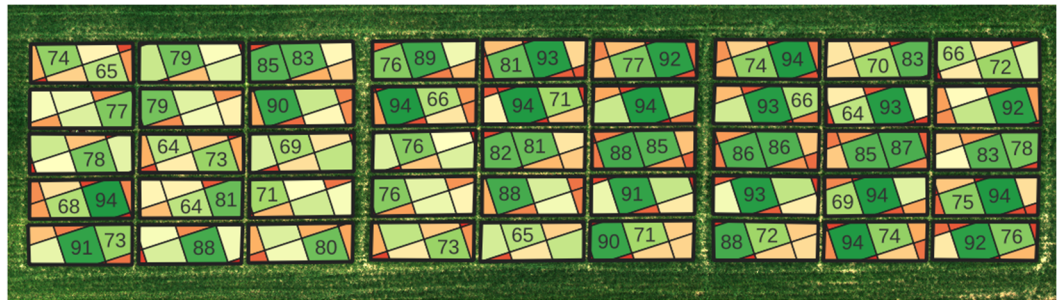
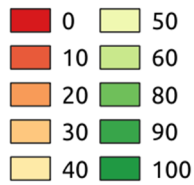
2.3. Remote Sensing Data

2.3.1. PlanetScope Imagery

PlanetScope is a commercial satellite constellation operated by Planet Labs, a company headquartered in San Francisco, California, USA. The constellation consists of approximately 180 satellites. Each satellite is a CubeSat 3U form factor ($10 \times 10 \times 30$ cm), capable of imaging the entire Earth's surface at a daily time step. The latest generation of PlanetScope sensors, known as Super Dove or PSB.SD, were used in this study. This generation produces near-daily images from March 2020 at 3 m spatial resolution and over 8 spectral bands (Supplementary Material: Figure S1 and Table S2) [49]. The band radiometry, the band spectral response, and the image sharpness have been significantly improved compared to the previous generations.

To develop this study, the Analytic Ortho Scene product was downloaded from October 2022 to August 2023 considering a total of 100 cloud-free surface reflectance images. The Ortho Scene product is an orthorectified surface reflectance product (level 3B), radiometrically, geometrically, and atmospherically corrected. Orthorectification was performed to correct terrain-induced distortions using high-quality digital elevation models (DEMs) with a post-spacing of 30–90 m. Ground control points (GCPs) were integrated to enhance geolocation accuracy, with precision depending on the density and quality of available GCPs in the region. For geometric corrections, computer vision algorithms, including OpenCV's STAR keypoint detector and FREAK keypoint extractor, were utilized to detect feature points [50]. Radiometric calibration was applied to ensure the pixel values accurately represented surface reflectance. The imagery was captured in 16-bit depth, providing a high level of detail for spectral analysis. Atmospheric corrections were performed using the 6SV2.1 radiative transfer code to account for effects such as aerosol scattering and water vapor absorption [51]. Key atmospheric inputs, including aerosol optical depth (AOD), water vapor, and ozone levels, were retrieved from MODIS near-real-time datasets (MOD09CMA [52], MOD09CMG [53], and MOD08-D3 [54]). Analysis using PlanetScope images was performed at the pixel level due to the small size of the experimental plots (Figure 2). However, given the limited size of the experimental plots and their rectangular geometry that was not aligned with the pixel orientation, none of the PlanetScope pixels purely observed any of them, providing a mixed signal. Thus, only the pixels observing >85% of a given experimental plot were selected, resulting in a total of 21 pixels, covering at least one pixel each treatment.

Planet Percentage Signal



Planet pixel feasibility

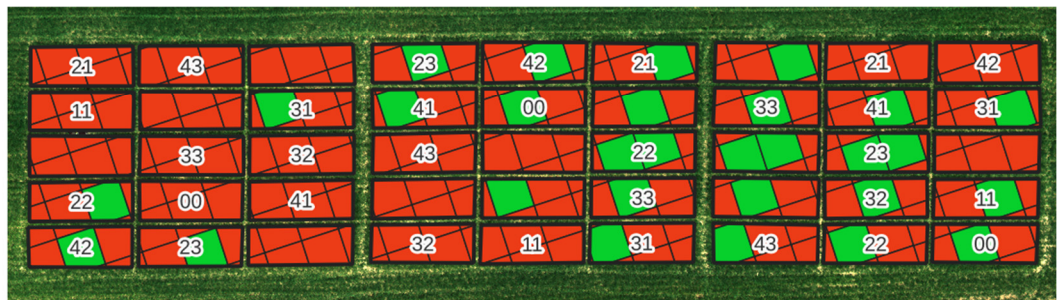
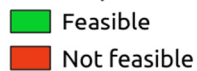


Figure 2. The rectangles represent each experimental plot while the squares represent PlanetScope pixels. The numbers highlight the proportion of pixel area inside each experimental plot, with a gradient color from red (almost no area in the plot) to green (mostly inside the plot). In the bottom figure, the 21 pixels that fit into the experiment plot (enumerated fields) are highlighted in green.

2.3.2. UAV Data

Multi-temporal flights using an Inspire a UAV quadcopter type DJI[®] Inspire 1 (SZ DJI Technology Co., Ltd., Shenzhen, China) were conducted over the experimental site (1080 m²) where multispectral images were taken on three different dates (19 January, 22 March and 10 May) during the wheat growing season. Flights were conducted under conditions of low wind speed, partly cloudy skies, and good visibility. Perpendicular flights were made at 50 m height to create a grid covering each plot and its surroundings (90% overlap between flight lines). A multispectral camera was acquired in five spectral bands (Supplementary Material: Figure S1 and Table S2) by MicaSense (MS) RedEdge-M sensor (1.2 Mpx and 5.4 mm focal length) was used to acquire the information attached to the rear from Inspire 1 DJI UAV, using a custom mounting plate and independently powered by an external battery. Images captured by the the RedEdge-M were sorted as 16-bit RAW tiff files. MS images were processed using the Pix4D v4.6.4[®] software. An orthomosaic was generated using Structure from Motion (SfM) techniques, which reconstruct 3D geometry and spatial alignment from overlapping images [55]. This process included feature matching, bundle adjustment, and dense point cloud generation to ensure high spatial accuracy and seamless image stitching. The resulting orthomosaic was georeferenced using real-time kinematic (RTK) GPS points for precise alignment with the experimental site. This software was also utilized to process the MS images, transforming the raw digital data into radiance and reflectance. Calibration of the MS imagery was performed using the camera's standard calibrated white reflectance panel. The radiometric calibration process follows the equation provided by MicaSense [56], shown as (Equation (1)), which is based on their official radiometric conversion model:

$$L_{sen\lambda} = V_{(x,y)} \times \left(\frac{a_1}{g} \right) \times \frac{p - p_{BL}}{t_e - a_2y - a_3t_e y} \quad (1)$$

where L_{sen} is the spectral radiance at wavelength λ ; $V_{(x,y)}$ is the vignette polynomial function at pixel (x,y) ; a_1 , a_2 , and a_3 are the radiometric calibration coefficients; g is the sensor gain setting; p is the normalized DN value; p_{BL} is the black level offset; and t_e is the image exposure time. All parameters required for radiance calculation are provided

in the image metadata. After determining the radiance, the reflectance is derived using the calibrated white reflectance panel and the function supplied by MicaSense [57]. This computation relies on a standard reflectance panel captured from an image taken at a height of 1 m. The corresponding formula is presented in Equation (2):

$$F_{i\lambda} = \frac{\rho_{i\lambda}}{\frac{1}{n} \sum_{j=1}^n L_{i,j\lambda}} \quad (2)$$

where $\rho_{i,\lambda}$ is the panel's reflectance at wavelength λ , and $L_{i,\lambda}$ represents the radiance measured for the j -th pixel of the reflectance panel.

Once this conversion factor ($F_{i,\lambda}$) is determined, the reflectance at wavelength λ (ρ_λ) for the image can be calculated by multiplying the spectral radiance by the conversion factor, as shown in Equation (3):

$$\rho_\lambda = L_{sen\lambda} \times F_{i\lambda} \quad (3)$$

After radiometric calibration, MS images were orthorectified using geodetic coordinates from Real Time Kinect GPS GNSS RTK (Emlid, Reach RS2) using the control ground points obtained on the edge of plots, using the georeference tool from QGIS 3.36 software [58]. The pixel resolution of the processed images was 2.0 cm.

2.4. Crop Variables Estimation Using Remote Sensing Data

In this experiment, we conducted a comparative analysis of different measurements across different treatments and explored their relationships with remote sensing spectral bands or vegetation indexes. In the following sections, we examine phenological metrics, vegetation cover fraction, and key components such as crop yield, starch content, and protein content using MS and PS datasets.

2.4.1. Phenological Metrics Extraction

The phenological metrics extracted in this study included the start of the season (SOS), length of the season (LOS), peak of the season (POS), and end of the season (EOS). These metrics were derived from the Normalized Difference Vegetation Index (NDVI) [59,60] time series of the study area. A Savitzky–Golay filter [61] was applied to minimize noise in the time series. The phenological metrics were determined based on the temporal evolution of the NDVI time series [25] and percentile extraction: The NDVI maximum was identified as the POS, the SOS was defined as the 10th percentile of NDVI values preceding the maximum, and the EOS was defined as the 10th percentile of NDVI values following the maximum. LOS was calculated as the difference in days between the EOS and the SOS. These derived phenological metrics were then compared with the phenological calendars recorded during the experiment, and any discrepancies were noted.

In addition to these phenological metrics, the accumulated growing degree days (GDD_{accum} , Equation (4)) were also considered to provide a more comprehensive understanding of crop development in the study area. GDD_{accum} is a measure of heat accumulation, which directly influences the timing of key phenological stages such as germination, flowering, and maturity [62]

$$GDD_{accum} = \sum_{d=SOS}^{EOS} \left(\frac{T_{max} + T_{min}}{2} \right) - T_{base}0 \quad (4)$$

where T_{max} , T_{min} , and T_{base} are the maximum, minimum, and base temperatures, respectively. In the case of winter wheat, the T_{base} is 0 °C. By considering the cumulative temperature exposure throughout the growing season, GDD_{accum} provides a more accurate prediction of phenological events than calendar days alone [63]. Once the phenological metrics were calculated, the accumulation of GDD began from SOS and continued until EOS. This approach allowed temperature data to be integrated throughout the growing season, providing a normalized evolution for crop development. The GDD_{accum} between

SOS and EOS allowed us to quantify the heat accumulation required for the progression of phenological stages, thereby providing insight into the relationship between temperature and vegetation dynamics. This GDD_{accum} , in conjunction with the previously derived phenological metrics, was compared with the Zadock (Z) crop development recorded in the experiment.

2.4.2. Fraction of Green Vegetation Cover

The evolution of fCover was measured in situ on four specific dates (1 January, 12 February, 22 March, and 10 May) corresponding to key stages in the crop growth, including sowing and grain development mentioned in Section 2.2. These dates were chosen to capture the dynamic changes in vegetation cover during the growing season. The in situ measurements were then compared with the remote sensing data, specifically, the vegetation indices in Table 2, calculated for both PS and MS datasets. For vegetation indexes, we established linear relationships between the in situ vegetation cover measurements and the PS and MS indexes. In the case of PS, the evolution of the whole time series over the growing season was analyzed to investigate how different treatments affected the vegetation cover at different phenological stages. This analysis provided insights into the temporal dynamics of vegetation cover and the impact of different treatments on crop development, as observed from both ground measurements and remote sensing data.

Table 2. Calculated vegetation indices based on the blue, green, red, red edge (RE) and near infrared (NIR) spectral bands of the PlanetScope instrument or MicaSense multispectral camera.

Index	Formula	Reference
RVI	$\frac{NIR}{Red}$	[64]
DVI	$NIR - Red$	[59,60]
NDVI	$\frac{NIR - Red}{NIR + Red}$	[59,60]
SAVI	$\frac{(NIR - Red) * 1.5}{NIR + Red + 0.5}$	[65]
WDVI	$NIR - 0.5 * Red$	[66]
GNDVI	$\frac{NIR - Green}{NIR + Green}$	[67]
MCARI	$[(RE - Red) - 0.2(RE - Green)] \left(\frac{RE}{Red} \right)$	[68]
EVI	$2.5 \frac{NIR - Red}{(NIR + 6 * Red - 7.5 * Blue) + 1}$	[69]
TRBI	$\frac{Green + Red}{NIR}$	[70]
NDI45	$\frac{RE - Red}{RE + Red}$	[71]
SeLI	$\frac{NIR - RE}{NIR + RE}$	[72]

Validation of vegetation cover predictions was conducted using standardized metrics to assess model performance. These included the coefficient of determination (R^2), which measures the strength of the relationship between observed and predicted values; the mean of the residuals (bias), which evaluates systematic deviations; the standard deviation of the residuals (σ), which quantifies data spread; and the root mean square error (RMSE), which assesses overall accuracy. These metrics were applied to compare predicted and observed fractional vegetation cover values across different treatments and phenological stages.

2.4.3. Harvest Components, Crop Yield, and Quality

Estimates of crop yield, protein content, starch, and hectoliter weight obtained at harvest were analyzed by examining the relationships between these components and combinations of two spectral bands from the drone and satellite datasets. A linear model was applied to quantify these relationships at various phenological stages of the crop, incorporating accumulated growing degree days (GDD) from the start of the season (SOS) to the specific date corresponding to each stage. The model is expressed as

$$Harvest\ component = m_1 \rho_{\lambda 1_{GDD}} + m_2 \rho_{\lambda 2_{GDD}} + n \quad (5)$$

where $\rho_{\lambda_1, GDD}$ and $\rho_{\lambda_2, GDD}$ represent the reflectance values for bands λ_1 and λ_2 at a given GDD, m_1 and m_2 are coefficients for each band, and n is the intercept. This approach allowed us to evaluate how well spectral data captured key crop traits at different growth stages.

The study focused on identifying phenological stages, particularly those before the peak of the growing season, that exhibited the strongest correlations with spectral data. This approach aimed to evaluate the potential for predicting crop components, including yield, protein content, starch, and hectoliter weight, using satellite- and drone-derived data. Validation was performed by comparing remotely sensed data with ground-based measurements, using metrics such as the coefficient of determination (R^2), mean residuals (*bias*), standard deviation of residuals (σ), and root mean square error (RMSE). These metrics were applied consistently with the validation framework described for vegetation cover predictions.

3. Results

3.1. Vegetation Dynamics Monitored by Remote Sensing

The development of winter wheat represented by the average NDVI as recorded by PlanetScope (PS), is shown in Figure 3. The NDVI time series effectively tracks the key phenological stages of the crop, with the SOS, POS, and EOS marked by their respective indicators. The progression of GDD is shown on the x-axis, corresponding to the timeline of the study. Based on actual observations, the start of the season (SOS) was on 18 November 2022, and the end of the season (EOS) was on 27 June 2023. PlanetScope satellite estimates detected the SOS on 26 November 2022, underestimating the actual date by 8 days, and the EOS on 15 June 2023, overestimating the actual date by 12 days compared to the sowing and harvest, respectively.

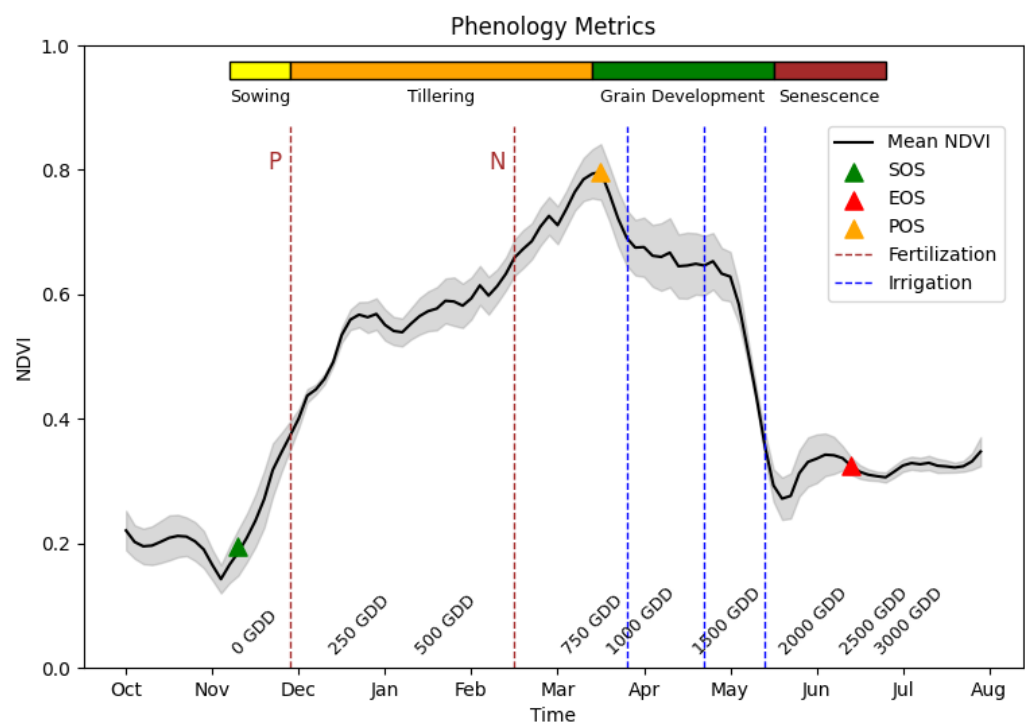


Figure 3. Winter wheat temporal dynamics of NDVI and GDD across different phenological stages.

In the early stages, corresponding to the sowing stage (Z_0), the crop starts to emerge in early November 2022. At this stage, the accumulated GDD ranged from 0 to 440 GDD, and the NDVI ranged from a minimum of 0.11 to a maximum of 0.54, with a mean value of 0.31 (Table 3). As the crop progresses into the tillering stage ($Z_{2,3}$) between mid-December 2022 and late January 2023, the NDVI steadily increases, indicating additional wheat tillers.

During this period, the cumulative GDD ranged from 464 to 884, and the NDVI increased from a minimum of 0.36 to a maximum of 0.69, with a mean value of 0.52. The peak NDVI values occur during the grain development stage ($Z_{7,1}$), which extends from the end of March to the end of May 2023. At this time, the crop reaches maximum vegetative growth, with GDD_{accum} ranging from 1004 to 1911. The NDVI at this stage increases to an average of 0.62, with a maximum of 0.77. Finally, the senescence stage ($Z_{9,3}$) occurs from late May to June 2023 and marks the decline in NDVI as the crop matures. During senescence, the GDD_{accum} ranges from 1928 to 2505, while the NDVI values drop from a maximum of 0.46 to a minimum of 0.19, with a mean value of 0.30.

Table 3. NDVI and GDD summary for different phenological metrics.

Phenology	Min GDD	Mean GDD	Max GDD	Min NDVI	Mean NDVI	Max NDVI
Sowing ($Z_{0,0}$)	0	277	440	0.11	0.31	0.54
Tillering ($Z_{2,3}$)	464	607	884	0.36	0.52	0.69
Grain development ($Z_{8,7}$)	1004	1406	1911	0.38	0.62	0.77
Senescence ($Z_{9,0}$)	1928	2340	2505	0.19	0.30	0.46

In addition to the NDVI evolution, a comparative analysis between the MicaSense and PlanetScope reflectance values was conducted based on coincident acquisition dates (Supplementary Material: Figures S2 and S3). Figure S2 illustrates notable differences in RGB and NDVI values, with MicaSense providing higher spatial detail but differing NDVI ranges. Scatterplots in Figure S3 quantify these discrepancies, showing low R^2 values for individual acquisition dates, particularly in the blue and green bands ($R^2 < 0.25$). However, the overall R^2 improves when combining data across all dates, especially in the NIR band ($R^2 = 0.70$), capturing seasonal variability but not per-date agreement. In the MicaSense images, reflectance values are consistently lower than those from PlanetScope, with significant deviations in March and May. In fact, the scatter plots (Figure S3) further illustrate the weak correlation between MicaSense and PlanetScope reflectance, particularly in the blue and green bands, where Pearson's R^2 values are as low as 0.06 in January and 0.10 in May. Despite this, some bands, such as the red edge and NIR bands, show slightly better correlations, although the overall R^2 values remain below 0.30 across all acquisition dates. These discrepancies can be attributed to several factors, including differences in the relative spectral responses of the sensors and possible variations in the radiometric calibration procedures. Nevertheless, the overall relationship between the two sensors reflectance values is relatively weak.

The PlanetScope time series evolution of NDVI for the different treatments is shown in Figure 4. As observed, the NDVI trends differ significantly between the control and the different experimental treatments, especially after the fertilizer application. After the phosphorus application, the NDVI values show a significant increase, especially in treatments such as P(MAP) + N(Urea) and STr + C + N(Urea), which obtained the highest yields and maximum NDVI values, with peaks close to 0.6. In contrast, the control treatment shows a lower NDVI increase, peaking at around 0.5. After the nitrogen application, all treatments show a continuous upward trend in NDVI and reach their maximum values. After reaching their peak, the treatments can be divided into three groups: the high yield treatments maintain NDVI values around 0.8, the medium yield treatments stabilize around 0.75, and the lower yield treatments, including the control and the P(BM + C) + N(Urea) treatment, show NDVI values around 0.65. As the crop enters senescence, the NDVI values decrease sharply, eventually stabilizing between 0.3 and 0.4 at the end of the season.

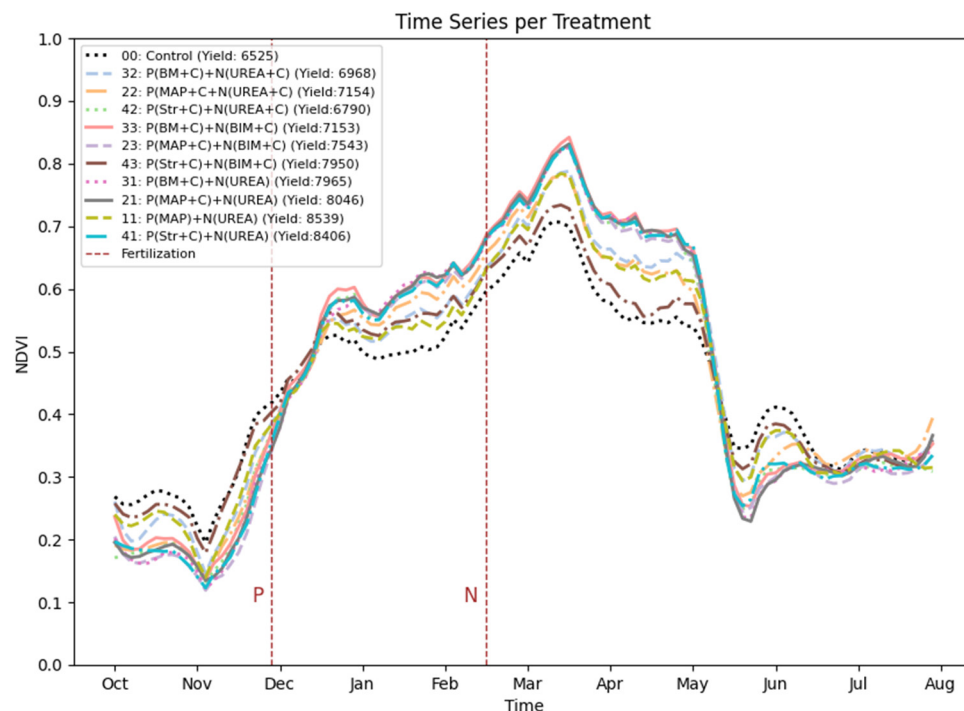


Figure 4. PlanetScope NDVI time series per each experiment.

A detailed comparison of NDVI values and rankings between MicaSense and PlanetScope across all treatments highlights both consistencies and discrepancies in sensor performance (Table S3). High-yield treatments such as P(St) + N(i) and P(Bm) + N(om) exhibit strong agreements, with MS NDVI values averaging 0.590 and 0.586 compared to PS 0.676 and 0.664, respectively, and minimal ranking differences of 1 to 2 ranks. However, mid-yield treatments like P(Bm) + N(o), with average yields ranging between 6500 to 7500 kg ha⁻¹, reveal more notable differences, with PlanetScope ranking them higher on average by two to three ranks compared to Micasense. Across all treatments, 13 plots differ by only up to two ranks, but five show larger discrepancies, with differences exceeding three ranks, particularly for mid-range yield treatments. This reflects consistent alignment for extreme yields but suggests that mid-yield treatments exhibit greater variability in rankings between the two sensors.

3.2. Fraction of Vegetation Cover

The performance of the top five fCover prediction models, using data derived from both the PlanetScope and MicaSense sensors, and the scatter plot of the best model are shown in Figure 5. The PlanetScope model, using the Enhanced Vegetation Index (EVI), showed a correlation of $R^2 = 0.68$ with the measured fCover values. The standard deviation between the different treatments was relatively small, indicating limited variability in the predictions. The MicaSense model, using the Normalized Difference Vegetation Index (NDVI), showed a higher correlation with measured fCover values ($R^2 = 0.82$, RMSE = 8.3%). The standard deviation in PlanetScope between the different treatments indicates limited sensitivity to the variations induced by different agronomic practices, such as fertilization with phosphorus and nitrogen. This lack of variability in PlanetScope predictions is probably due to its coarser spatial resolution, which may not capture the heterogeneity present in the experimental plots. The MicaSense model also showed greater variability in both measured and predicted values, as indicated by the larger standard deviations across the treatments. This increased variability likely to reflect the higher spatial resolution of the MicaSense sensor, which is better able to capture the finer scale variations in crop cover caused by different treatments. The improved agreement and variability in MicaSense

predictions suggests that it may be more effective for monitoring fCover in heterogeneous experimental conditions.

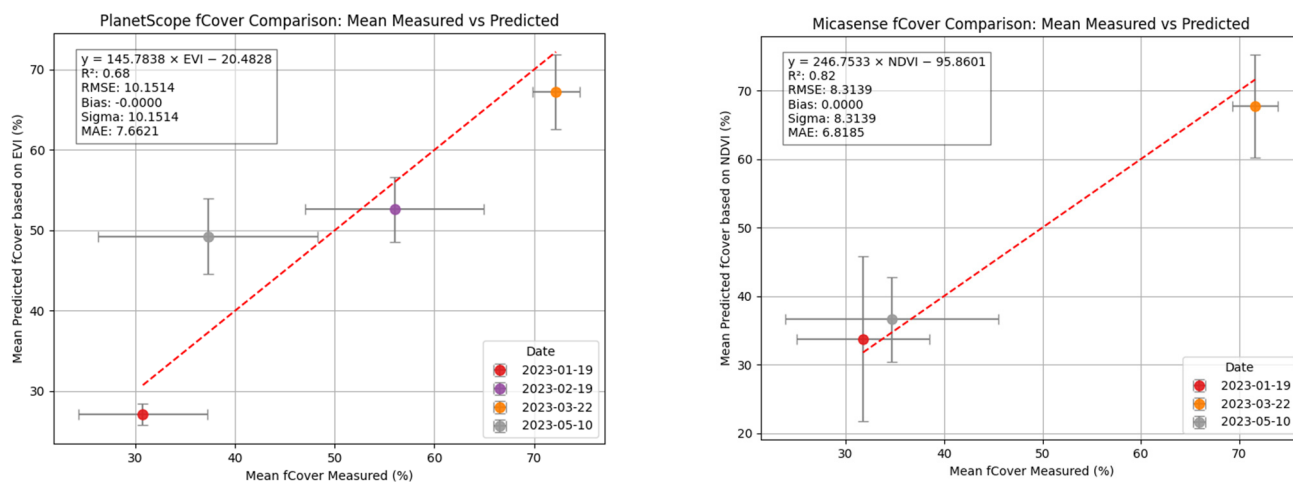


Figure 5. Comparison of measured and predicted fCover using PlanetScope and Micasense.

Time series analysis of fCover, based on PlanetScope Enhanced Vegetation Index (EVI), shows the seasonal dynamics of vegetation cover across the different experimental treatments (Supplementary Material: Figure S4). The control treatment (plot 00, see Table 1), which did not receive fertilization, consistently shows the lowest fCover values throughout the growing season, indicating minimal vegetative growth. In contrast, the phosphorus and nitrogen fertilized treatments show varying degrees of increased vegetation cover. For example, treatments with P(MAP) + N(Urea) (plot 11) and P(Str + C) + N(Urea) (plot 42) show higher fCover values, especially during the peak of the growing season.

3.3. Harvest Components: Crop Yield, Protein Content, Starch, and Hectoliter Weight

The crop yield and grain quality parameters showed significant differences ($p < 0.0001$) between fertilizing treatments (Table 4). All the fertilized plots had higher yields than the unfertilized control plots. We can observe that the highest performance was obtained in the plots fertilized with conventional strategies P(MAP) + N(Urea) (8618 kg ha^{-1}), followed by P(Str + C) + N(Urea), which showed a similar yield compared to the inorganic treatment. The fertilizers applied significantly increased the protein content (+31.6%) and HW (5%) in grain compared to the unfertilized control. P fertilization combined with N treatments, N(Urea) and N(Urea + C), showed a more positive effect on the protein content and HW than N(BM + C). On the contrary, starch was significantly higher in the unfertilized control, followed by P(BM + C)+N(Urea + C).

Table 4. Analysis of variance (ANOVA) of wheat yield components for fertilizer treatments in the 2022/2023 growing season.

Treatment	Plot	Grain Yield (kg ha ⁻¹)	HW (kg hL ⁻¹)	Grain Protein (%)	Starch (%)
Control	00	6429 a	75.4 a	7.6 a	77.95 c
P(MAP) + N(Urea)	11	8618 g	79.4 c	10.6 de	70.37 ab
P(MAP + C) + N(Urea)	21	7708 def	79.7 c	11.1 e	64.55 a
P(MAP + C) + N(Urea + C)	22	7524 cde	79.3 c	10.1 cd	71.42 abc
P(MAP + C) + N(BIM + C)	23	6993 bc	78.2 b	9.2 b	67.03 ab
P(BM + C) + N(Urea)	31	7965 ef	79.7 c	10.6 de	66.98 ab
P(BM + C) + N(Urea + C)	32	7219 bcd	79.3 c	10.5 de	72.51 bc
P(BM + C) + N(BIM + C)	33	6823 ab	79.0 bc	9.0 b	68.04 ab
P(Str + C) + N(Urea)	41	8183 fg	79.7 c	9.6 bc	67.9 ab
P(Str + C) + N(Urea + C)	42	7761 def	79.5 c	10.2 cd	66.79 ab
P(Str + C) + N(BIM + C)	43	7068 bc	79.1 c	9.2 b	66.19 ab
<i>p</i> -Value		***	***	***	***

HW: Hectoliter weight. ***: significant difference between treatments at $p < 0.0001$. Different letters within a column indicate significant differences between treatments ($p < 0.05$). Values indicate mean ($n = 3$). For acronyms, see Table 1.

Figures 6 and 7 show the analysis of key crop components—such as yield, protein content, starch, and hectoliter weight—which are modeled using PlanetScope and MicaSense data based on specific spectral bands. The timing of fertilization with phosphorus (P) plays a key role in influencing these results, as reflected in the phenological data at the beginning of the season. The PlanetScope model showed moderate correlations between predicted and actual values for the different crop components. For crop yield monitoring, the PlanetScope model showed an R^2 of 0.54, with the best predictions occurring during phases of rapid plant growth after fertilization. The model used spectral bands B04 (green)-B06(red) with a GDD of 569 (Figure 6a). For starch content, the PlanetScope model achieved an R^2 of 0.56 using bands B04 (green)-B08 (NIR) with a GDD of 761 (Figure 6b), effectively capturing starch accumulation, particularly after nitrogen application at tillering. HW, an indicator of grain quality, showed an $R^2 = 0.51$ with bands B02 (blue)-B07 (red edge) (GDD of 414) (Figure 6d). The consistency in predicting HW suggests that early phosphorus and nitrogen fertilization helped to maintain grain density. Protein content showed a slightly lower correlation ($R^2 = 0.49$) using bands B02 (blue)-B06 (red edge) and a GDD of 554 (Figure 6c).

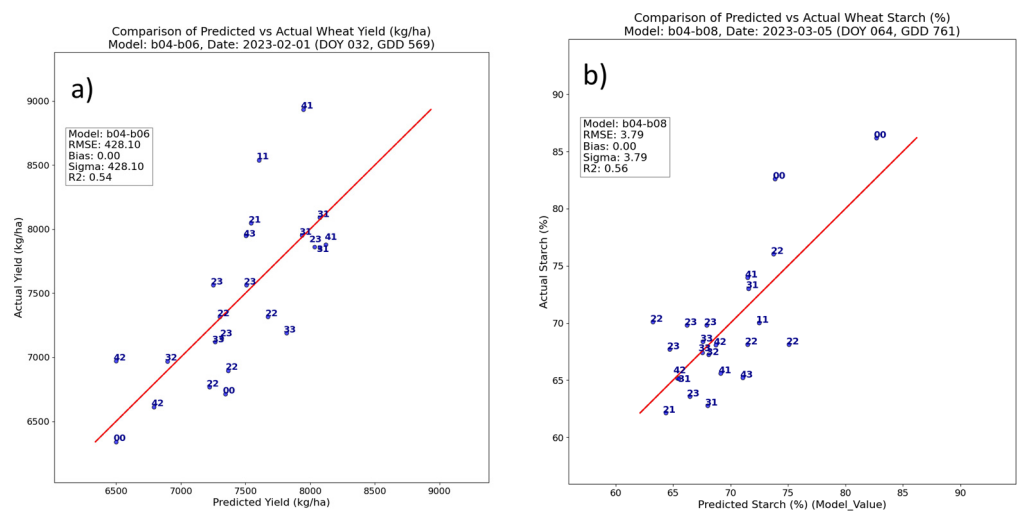


Figure 6. Cont.

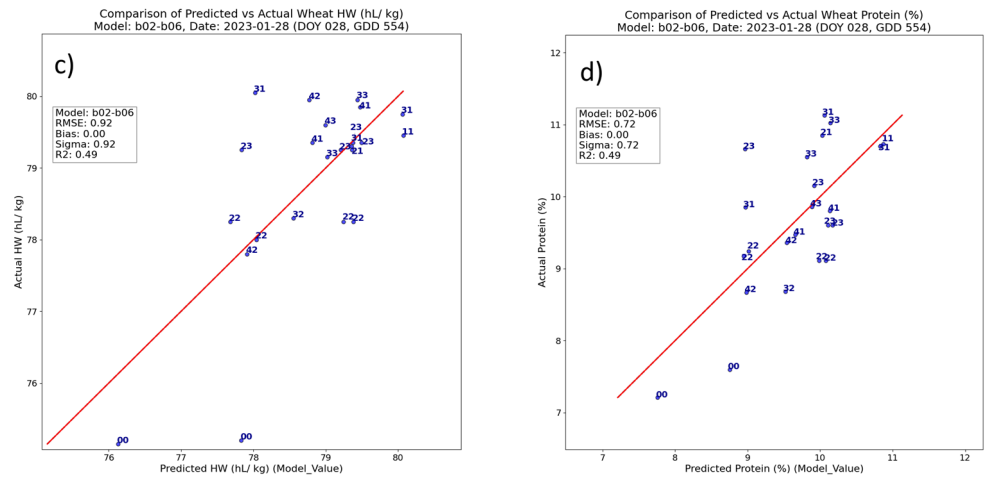


Figure 6. Comparison of predicted and actual wheat components using PlanetScope data. (a) Yield (kg ha^{-1}), (b) starch content (%), (c) protein content (%), and (d) hectoliter weight (hL kg^{-1}).

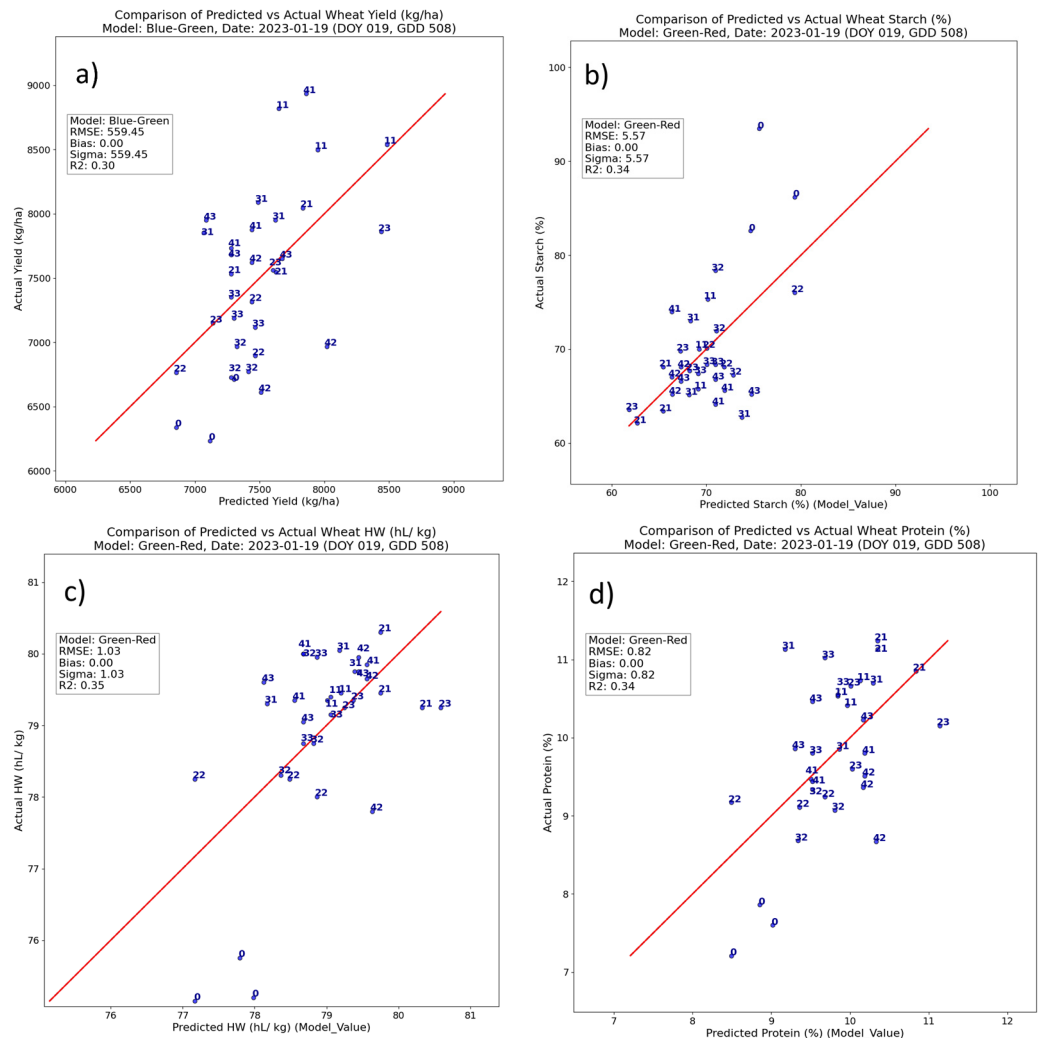


Figure 7. Comparison of predicted and actual wheat components using RedEdge-M data. (a) Crop yield (kg ha^{-1}), (b) starch content (%), (c) protein content (%), and (d) hectoliter weight (hL kg^{-1}).

In contrast, the MicaSense sensor performed poorly for all crop components (Figure 7). The correlation between the predicted and actual values was weak for crop yield ($R^2 = 0.30$), starch content ($R^2 = 0.34$), hectoliter weight ($R^2 = 0.35$), and protein content

($R^2 = 0.34$). These low R^2 values indicate that the MicaSense model struggled to capture meaningful linear relationships between the spectral data and the measured outcomes in this experiment.

4. Discussion

4.1. Phenology Metrics and Thermal Evolution

The use of PlanetScope imagery in this study has proved effective in monitoring the phenological development of winter wheat. The alignment of NDVI values with key phenological stages, as outlined by the Zadoks scale, suggests that satellite-derived data can provide accurate insights into the temporal dynamics of crop growth. The detection errors associated with SOS and EOS (8 days and 12 days, respectively) are acceptable given the scale of remote sensing data and its inherent temporal resolution. Also, note that the field-level SOS represents the sowing date, while the SOS derived from remote sensing corresponds to the crop's emergence. As expected, this remote sensing-based SOS is detected later than the sowing date. Similarly, for EOS, the satellite detected the end of the season sooner than the actual date observed in the field, likely due to differences in how crop senescence is captured from satellite data compared to ground-based observations. These results highlight the ability of PlanetScope's high temporal resolution to effectively track vegetation dynamics, allowing accurate detection of phenometrics such as SOS and EOS. PlanetScope's frequent revisits provide a significant advantage in capturing rapid temporal changes in crop development, ensuring that key phenological stages are accurately monitored throughout the growing season. Previous studies have emphasized the importance of temporal resolution for accurately capturing land surface phenology metrics, further supporting the effectiveness of PlanetScope in addressing these challenges [73].

Furthermore, the steady increase in NDVI during tillering and the sharp increase leading up to grain development demonstrate the sensitivity of NDVI to changes in biomass and canopy cover. The correlation between NDVI and GDD further supports the use of remote sensing data to predict key phenological events, which could help to optimize agricultural management practices, such as fertilizer application and irrigation scheduling. The results show a clear correlation between the satellite-derived NDVI values, the phenological stages described by the Zadoks scale, and the accumulation of GDD. The NDVI patterns and their relationship with GDD provide a robust framework for understanding winter wheat development throughout the growing season.

The combination of thermal time models, such as GDD, and observations based on the Zadoks scale is particularly valuable in capturing the full complexity of crop development. While GDD provides a continuous, temperature-driven metric that can be applied to different agroecosystem conditions [74], the Zadoks scale provides detailed insights into specific phenological stages, which are critical for local field management. As highlighted by Li et al. (2023) [75], GDD and other thermal indices are more easily scalable over larger regions, making them ideal for remote sensing applications, while the Zadoks scale remains critical for precise, site-specific observations. The integration of both approaches improves the accuracy of phenological monitoring and ensures a comprehensive understanding of crop growth dynamics under varying environmental conditions.

The observed changes in NDVI across the phenological stages provide valuable insight into the relationship between biomass accumulation and thermal time. During the early stages of development, the NDVI effectively captures the initial vegetative growth, reflecting the sensitivity of remote sensing data to small increases in canopy cover. As the crop transitions into the tillering and grain development stages, the strong correlation between NDVI and GDD highlights the ability of thermal time models to predict key phenological events and canopy dynamics. Similar GDD ranges have been reported in other studies investigating winter wheat development, confirming the scalability of GDD as a reliable metric for monitoring crop growth [76]. The sharp decline in NDVI during senescence clearly marks the onset of crop maturity, with GDD continuing to accumulate even as vegetative growth slows. This relationship between decreasing NDVI and increasing GDD

underscores the importance of integrating both thermal and spectral data for accurate phenological monitoring. These findings suggest that combining GDD and NDVI can be a powerful approach for optimizing agricultural management practices, especially for determining the ideal timing for interventions such as fertilizer application and harvest.

4.2. PlanetScope and MicaSense Intercomparability

The discrepancies in the correlation between PlanetScope and MicaSense reflectance values, as highlighted by the low Pearson R^2 values across the spectrum, are largely due to the fundamental differences in their spectral responses. The two sensors are designed with different band specifications and sensitivities. The PS SSD sensor captures a wider range of wavelengths compared to the RedEdge-M sensor, which has narrower and more defined spectral bands. This mismatch in wavelength coverage and bandwidth is likely to lead to variations in the measured reflectance, particularly in regions of the spectrum where the two sensors do not fully overlap. In addition, differences in radiometric calibration procedures between the two sensors may further contribute to the observed discrepancies. These findings align with previous reports of MicaSense camera limitations, particularly, the underestimation of the reflectance values for reference panels and the challenges associated with sensor saturation [77] and band [78] mismatch. Consequently, direct comparisons between the two datasets should account for these inherent differences in spectral characteristics and calibration methods.

When such variability cannot be resolved by addressing biases alone, incorporating ground-based surface reflectance measurements becomes critical. These measurements provide an objective reference to evaluate uncertainties and validate reflectance values from both satellite and drone data. For MicaSense, improvements in acquisition protocols, such as accounting for BRDF effects in the SfM workflow or correcting illumination-induced variability during flights, could reduce discrepancies. In contrast, PlanetScope benefits from being an Analysis Ready Data (ARD) product, with harmonized corrections for radiometry, geometry, and atmosphere. These preprocessing advantages ensure consistency, although validation using reference data remains essential.

Furthermore, although Leach et al. (2019) [79] reported radiometric uncertainties for PlanetScope arising from variations in acquisition times, additional challenges are presented by anisotropic variations related to the bidirectional reflectance distribution function (BRDF), as demonstrated by Roy et al. (2021) [80]. Such directional effects are exacerbated by differences in acquisition timing between sensors, potentially further complicating the comparison between PlanetScope and MicaSense data. However, the observed consistency in PlanetScope's SuperDove data can be attributed to the atmospheric correction applied to harmonize the constellation. This harmonization process has proven reliable in comparison with other datasets, such as Sentinel-2 [81,82], suggesting that while temporal and directional variations present challenges, the SuperDove's corrected data may mitigate some discrepancies when properly accounted for.

Additionally, a comparative analysis of NDVI rankings between MicaSense and PlanetScope revealed consistent alignment in high-yield treatments, such as P(St) + N(i) and P(Bm) + N(om), where differences in NDVI ranks were minimal, typically within one or two ranks. However, mid-yield treatments, such as P(Bm) + N(o), exhibited larger discrepancies, with PlanetScope ranking these treatments higher by two to three ranks on average. This suggests that while PlanetScope is effective in tracking broad trends in crop development, particularly in high-yield scenarios, mid-yield treatments demonstrate greater variability. This variability in MicaSense data could be attributed to challenges in radiometric calibration, which may have affected its ability to accurately detect finer-scale variability induced by different fertilization strategies.

4.3. fCover Retrieval Using Remote Sensing Dataset

The results show that while the PlanetScope-based models are useful for capturing general trends in fractional vegetation cover (fCover), they are limited in their ability

to discriminate finer-scale effects of different agronomic treatments. The relatively low standard deviations and moderate correlations suggest that the coarser spatial resolution of PlanetScope likely limits its ability to detect the subtle heterogeneity present within experimental plots. This limitation is particularly evident in treatments with varying levels of phosphorus and nitrogen fertilization, where spatial variability in plant cover is expected to be higher due to differential nutrient uptake. Among the PlanetScope indices, the Enhanced Vegetation Index (EVI) was the most effective predictor, yet it still exhibited limited sensitivity and may have underestimated the influence of certain treatments on crop cover.

Although the satellite-derived fCover models capture general seasonal trends, they have limitations in distinguishing between specific fertilization products and combinations. This is evident during the post-peak period, where fCover is often overestimated, particularly in treatments involving compost and nitrogen-based fertilizers. For example, treatments such as P(BM + C) + N(Urea) show higher modeled fCover than expected toward the later stages of the season. Despite these discrepancies, the fCover models effectively reflect overall temporal patterns of crop growth and provide useful insights into the relative effects of different fertilization strategies on vegetation development at the plot scale. However, the tendency to overestimate fCover in fertilized plots, especially those receiving higher nutrient doses (e.g., compost combined with urea), underscores one of the key limitations of the models.

In contrast, the superior performance of the RedEdge-M model, particularly in the Normalized Difference Vegetation Index (NDVI) model ($R^2 = 0.82$), can be attributed to the higher spatial resolution of the sensor, which allows for more accurate detection of fCover variability across experimental plots. This increased variability, reflected in the higher standard deviations, suggests that RedEdge-M can better capture the effects of different fertilizer treatments on crop cover, especially in the more heterogeneous parts of the field. For example, treatments involving compost and organic nutrient applications, which typically cause localized variations in soil fertility, are better detected by the RedEdge-M sensor. This increased sensitivity to within-field variability is critical for accurately monitoring crop response to nutrient treatments and improving precision farming strategies.

It is particularly noteworthy that NDVI, an index traditionally recognized for its ability to minimize directional effects, outperforms other indices from the RedEdge-M sensor. By utilizing the red and near-infrared (NIR) bands, NDVI may be less influenced by calibration problems, which could explain its superior performance in this study. This observation is especially intriguing given the earlier challenges encountered with MicaSense's calibration inconsistencies, as discussed in prior sections. Despite the sensor's known issues, NDVI's robustness appears to mitigate some of the calibration-related drawbacks, allowing for a more reliable detection of fCover variability in experimental plots.

Given the variability observed between the datasets, data fusion presents a promising avenue to enhance the synergistic analysis of vegetation dynamics. However, before implementing such approaches, it is essential to address the quality of surface reflectance measurements to improve intercomparability. Ensuring consistency in reflectance data through ground-based validation and addressing differences in radiometric calibration or acquisition protocols will provide a robust foundation for effective integration.

While the RedEdge-M sensor outperformed PlanetScope in terms of model accuracy and variability detection, it is important to note that both sensors still have limitations in their ability to perfectly predict fCover across all treatments. Factors such as environmental variability, differences in nutrient uptake efficiency, and potential sensor-specific biases may have contributed to the observed discrepancies. For example, the RedEdge-M model, while effective in detecting general variability, may still face challenges in capturing extreme treatment responses due to spectral limitations.

4.4. Harvest Components Models from Remote Sensing

The significant differences in yield components and quality parameters between fertilizing treatments reflect the expected effect of nutrient availability on crop growth and development. The high yields observed in plots treated with P(MAP) + N(Urea) and P(STR + C) + N(Urea) highlight the effectiveness of these fertilization strategies. The increase in protein content and hectoliter weight in response to N fertilization is consistent with known physiological responses in wheat, where late season N availability supports protein synthesis and improves grain quality. Interestingly, the unfertilized control had the highest starch content, suggesting that limited nitrogen availability may promote starch accumulation in grain, a finding consistent with previous studies on carbohydrate partitioning under nutrient-limited conditions [83,84].

The moderate performance of the PlanetScope model (R^2 from 0.49 to 0.56) suggests that while it can capture general trends in crop growth and yield, it may struggle to detect the finer-scale variability induced by different fertilization strategies due to its coarser spatial resolution. This limitation may affect its sensitivity to small-scale variations in crop cover and biomass often present in field trials. However, the model's ability to predict starch content ($R^2 = 0.56$) and hectoliter weight ($R^2 = 0.51$) demonstrates its potential for monitoring broad trends in crop quality, particularly over large-scale farms. These results highlight PlanetScope's value in leveraging high temporal resolution for identifying critical phenological stages, especially during rapid growth phases after fertilizer application, where predictions were strongest. For instance, starch content predictions effectively captured accumulation patterns driven by nitrogen application, while hectoliter weight predictions reflected the role of early-season phosphorus and nitrogen fertilization in maintaining grain density. These findings underscore the utility of PlanetScope in addressing the study's hypothesis, particularly, in enhancing precision and sustainability in crop management. In contrast, the poor performance of the MicaSense model ($R^2 < 0.30$) suggests that its spatial resolution and spectral sensitivity were insufficient to detect meaningful relationships between the experimental treatments and crop outcomes. The MicaSense sensor appeared to discriminate between the control and fertilized plots but was unable to detect the more subtle differences between different fertilization strategies. This limitation could be due to a combination of factors, including the sensor's reduced ability to capture variability, the problems of calibration, and its sensitivity to environmental conditions, that could interfere with accurate fCover retrievals.

Overall, while PlanetScope provided moderate predictions of yield components and crop quality, the MicaSense model was not effective in this context. The higher spatial resolution of MicaSense, which may be an advantage in other scenarios, did not translate into better prediction accuracy for yield components in this experiment. Nevertheless, in this experiment, the PlanetScope satellite constellation provides useful information for assessing the phenological development of winter wheat and yield retrieval at the plot scale.

5. Conclusions

This study demonstrates the critical role of integrating satellite and UAV remote sensing with sustainable fertilization strategies in optimizing winter wheat management under Mediterranean conditions. Fertilization had a significant impact on yield and quality, with P(MAP) + N(Urea) yielding 8618 kg ha^{-1} , outperforming other treatments. Organic-mineral fertilizers (OMFs) like P(STR + C)+N(Urea) showed performances comparable to those of inorganic options, reinforcing their potential as sustainable alternatives in high-yield agriculture while reducing environmental impacts.

The PlanetScope and MicaSense models showed mixed results in monitoring both fCover and yield components. PlanetScope performed reasonably well in predicting fCover ($R^2 = 0.68$), making it a valuable tool for capturing broad trends in crop cover across large-scale farms. However, its coarser spatial resolution limited its ability to detect the finer-scale variability induced by different fertilizer treatments. In contrast, the MicaSense

sensor, with its higher spatial resolution, performed better in retrieving fCover ($R^2 = 0.82$), demonstrating its potential for capturing more detailed vegetation cover changes.

When it came to predicting yield components and grain quality, including protein content, starch, and hectoliter weight, PlanetScope showed moderate correlations, with R^2 values ranging from 0.49 to 0.56, indicating its utility for the large-scale agricultural monitoring of broad trends in crop growth and quality. Specifically, it captured starch content with an R^2 of 0.56 and hectoliter weight with an R^2 of 0.51. In contrast, the MicaSense model struggled in this area, with R^2 values below 0.35 for yield and other crop quality metrics, suggesting its limitations for small plot analysis in this context. These findings emphasize the strengths of PlanetScope for broader-scale agricultural monitoring while highlighting the need for the further refinement of remote sensing tools like MicaSense to better capture crop-specific outcomes.

These findings underscore the importance of selecting the appropriate remote sensing tool based on the scale of analysis and precision requirements. While PlanetScope is proving effective for monitoring broad patterns at the field scale, integration with higher resolution sensors such as MicaSense or the use of advanced modelling techniques could improve prediction accuracy. This integration could improve the precision of treatment evaluation, leading to more informed agronomic decisions and promoting sustainable practices.

In the context of broader agronomy, the results highlight the potential of integrating organic-mineral fertilizers into modern agricultural systems to balance productivity and sustainability. These strategies align with global sustainability goals, such as those outlined in the EU's Farm to Fork initiative, which emphasizes reducing agriculture's environmental footprint while maintaining food security. Future research should focus on further refining data fusion approaches and developing tools to address discrepancies in monitoring crop components across varying spatial and temporal scales.

Supplementary Materials: The following supporting information can be downloaded at: <https://www.mdpi.com/article/10.3390/rs16234474/s1>, Table S1: Average climatological data during the trial; Figure S1: PlanetScope Superdove and Micasense RedEdge-M bands from SuperDove sensor; Table S2: PlanetScope & Micasense bands with their respective spectrum; Figure S2: RGB and NDVI from PlanetScope and Micasense-M during drone acquisitions; Figure S3: MicaSense and PlanetScope: bands comparisons with Pearson R^2 and RMSE (per date and overall); Table S3: Comparison of MicaSense and PlanetScope NDVI Values and Rankings Across Multiple Dates for Different Treatments; Figure S4: Time Series of fCover Modeled Using PlanetScope EVI Across Different Fertilization Treatments; Table S4: fCover prediction models for PlanetScope and Micasense RedEdge-M.

Author Contributions: Conceptualization, L.O. and R.M.; methodology, I.M.-L., B.F. and N.K.; software, I.M.-L. and K.C.; validation, S.S.-M. and I.M.-L.; formal analysis, L.O., I.M.-L. and K.C.; investigation, S.S.-M., M.Á.M.-U., F.J.A.-R. and J.A.S.-T.; resources, F.J.A.-R. and J.A.S.-T.; data curation, L.O. and R.M.; writing—original draft preparation, I.M.-L., K.C., L.O. and S.S.-M.; writing—review and editing, K.C., P.C.G. and N.K.; visualization, F.J.A.-R. and J.A.S.-T.; supervision, B.F. and N.K.; project administration, B.F. and R.M.; funding acquisition, B.F. and R.M. All authors have read and agreed to the published version of the manuscript.

Funding: This study forms part of the AGROALNEXT/2022/016 and COFRUT-MONITOR project (AGROALNEXT/2022/046) program and was supported by MCIN with funding from European Union NextGenerationEU (PRTR-C17.I1) and by Generalitat Valenciana. The study was funded by the program Generacio Talent of Generalitat Valencian (CIDEAGENT/2018/009) and Santiago Grisolia program (CIGRIS 2021/161), supported by the Conselleria d'Educació, Cultura, Universitats i Ocupació from Generalitat Valenciana.

Data Availability Statement: The data presented in this study are available on request from the corresponding authors.

Acknowledgments: The authors thank the NASA "Private-Sector Small Constellation Satellite Data Product Pilot Project" for providing access to the full Planetscope archive.

Conflicts of Interest: Author Pierre C. Guillevic was employed by the company Planet Labs Germany GmbH. The remaining authors declare that the research was conducted in the absence of any commercial or financial relationships that could be construed as a potential conflict of interest.

References

- Awika, J.M. Major cereal grains production and use around the world. In *Advances in Cereal Science: Implications to Food Processing and Health Promotion*; American Chemical Society: Washington, DC, USA, 2011; pp. 1–13.
- Sarwar, M.H.; Sarwar, M.F.; Sarwar, M.; Qadri, N.A.; Moghal, S. The importance of cereals (Poaceae: Gramineae) nutrition in human health: A review. *J. Cereals Oilseeds* **2013**, *4*, 32–35. [\[CrossRef\]](#)
- Asseng, S.; Ewert, F.; Martre, P.; Rötter, R.P.; Lobell, D.B.; Cammarano, D.; Kimball, B.A.; Ottman, M.J.; Wall, G.W.; Zhu, Y. Rising temperatures reduce global wheat production. *Nat. Clim. Chang.* **2015**, *5*, 143–147. [\[CrossRef\]](#)
- Barlow, K.M.; Christy, B.P.; O’Leary, G.J.; Riffkin, P.A.; Nuttall, J.G. Simulating the impact of extreme heat and frost events on wheat crop production: A review. *Field Crops Res.* **2015**, *171*, 109–119. [\[CrossRef\]](#)
- Powell, J.P.; Reinhard, S. Measuring the effects of extreme weather events on yields. *Weather Clim. Extrem.* **2016**, *12*, 69–79. [\[CrossRef\]](#)
- Song, Y.; Zhao, Y. Effects of drought on winter wheat yield in north China during 2012–2100. *Acta Meteorol. Sin.* **2012**, *26*, 516–528. [\[CrossRef\]](#)
- Chen, C.; Baethgen, W.E.; Robertson, A. Contributions of individual variation in temperature, solar radiation and precipitation to crop yield in the North China Plain, 1961–2003. *Clim. Chang.* **2013**, *116*, 767–788. [\[CrossRef\]](#)
- Zampieri, M.; Ceglar, A.; Dentener, F.; Toreti, A. Wheat yield loss attributable to heat waves, drought and water excess at the global, national and subnational scales. *Environ. Res. Lett.* **2017**, *12*, 064008. [\[CrossRef\]](#)
- Webber, H.; Ewert, F.; Olesen, J.E.; Müller, C.; Fronzek, S.; Ruane, A.C.; Bourgault, M.; Martre, P.; Ababaei, B.; Wallach, D. Diverging importance of drought stress for maize and winter wheat in Europe. *Nat. Commun.* **2018**, *9*, 4249. [\[CrossRef\]](#)
- Fang, H.; Baret, F.; Plummer, S.; Schaepman-Strub, G. An overview of global leaf area index (LAI): Methods, products, validation, and applications. *Rev. Geophys.* **2019**, *57*, 739–799. [\[CrossRef\]](#)
- Kamenova, I.; Dimitrov, P. Evaluation of Sentinel-2 vegetation indices for prediction of LAI, fAPAR and fCover of winter wheat in Bulgaria. *Eur. J. Remote Sens.* **2020**, *54* (Suppl. 1), 89–108. [\[CrossRef\]](#)
- Franch, B.; Vermote, E.; Skakun, S.; Santamaria-Artigas, A.; Kalecinski, N.; Roger, J.C.; Becker-Reshef, I.; Barker, B.; Justice, C.; Sobrino, J.A. The ARYA crop yield forecasting algorithm: Application to the main wheat exporting countries. *Int. J. Appl. Earth Obs. Geoinf.* **2021**, *104*, 102552. [\[CrossRef\]](#)
- Liu, S.; Hu, Z.; Han, J.; Li, Y.; Zhou, T. Predicting grain yield and protein content of winter wheat at different growth stages by hyperspectral data integrated with growth monitor index. *Comput. Electron. Agric.* **2022**, *200*, 107235. [\[CrossRef\]](#)
- European Commission. 2020. Available online: <https://ec.europa.eu/eurostat/web/products-eurostat-news/-/ddn-20220628-1> (accessed on 12 July 2024).
- Brown, S.; Cotton, M. Changes in Soil Properties and Carbon Content Following Compost Application: Results of On-farm Sampling. *Compos. Sci. Util.* **2011**, *19*, 87–96. [\[CrossRef\]](#)
- Sayara, T.; Basheer-Salimia, R.; Hawamde, F.; Sánchez, A. Recycling of Organic Wastes through Composting: Process Performance and Compost Application in Agriculture. *Agronomy* **2020**, *10*, 1838. [\[CrossRef\]](#)
- Papandrea, S.F.; Cataldo, M.F.; Palma, A.; Gallucci, F.; Zimbalatti, G.; Proto, A.R. Pelletization of Compost from Different Mixtures with the Addition of Exhausted Extinguishing Powders. *Agronomy* **2021**, *11*, 1357. [\[CrossRef\]](#)
- Chew, K.W.; Chia, S.R.; Yap, Y.J.; Ling, T.C.; Tao, Y.; Show, P.L. Densification of food waste compost: Effects of moisture content and dairy powder waste additives on pellet quality. *Process Saf. Environ. Prot.* **2018**, *116*, 780–786. [\[CrossRef\]](#)
- Sanz-Cobena, A.; Lassaletta, L.; Aguilera, E.; Prado, A.; del Garnier, J.; Billen, G.; Iglesias, A.; Sánchez, B.; Guardia, G.; Abalos, D.; et al. Strategies for greenhouse gas emissions mitigation in Mediterranean agriculture: A review. *Agric. Ecosyst. Environ.* **2017**, *238*, 5–24. [\[CrossRef\]](#)
- Kim-Ho, T.T.; Tra, V.T.; Le, T.H.; Nguyen, N.K.-Q.; Tran, C.S.; Nguyen, P.T.; Vo, T.D.H.; Thai, V.N.; Bui, X.T. Compost to improve sustainable soil cultivation and crop productivity. *Chem. Environ. Eng.* **2022**, *6*, 100–211.
- Becker-Reshef, I.; Vermote, E.; Lindeman, M.; Justice, C. A generalized regression-based model for forecasting winter wheat yields in Kansas and Ukraine using MODIS data. *Remote Sens. Environ.* **2010**, *114*, 1312–1323. [\[CrossRef\]](#)
- Pasqualotto, N.; Delegido, J.; Van Wittenberghe, S.; Rinaldi, M.; Moreno, J. Multi-crop green LAI estimation with a new simple Sentinel-2 LAI Index (SeLI). *Sensors* **2019**, *19*, 904. [\[CrossRef\]](#)
- Sishodia, R.P.; Ray, R.L.; Singh, S.K. Applications of remote sensing in precision agriculture: A review. *Remote Sens.* **2020**, *12*, 3136. [\[CrossRef\]](#)
- Gao, L.; Wang, X.; Johnson, B.A.; Tian, Q.; Wang, Y.; Verrelst, J.; Mu, X.; Gu, X. Remote sensing algorithms for estimation of fractional vegetation cover using pure vegetation index values: A review. *ISPRS J. Photogramm. Remote Sens.* **2020**, *159*, 364–377. [\[CrossRef\]](#) [\[PubMed\]](#)
- Caparros-Santiago, J.A.; Rodriguez-Galiano, V.; Dash, J. Land surface phenology as indicator of global terrestrial ecosystem dynamics: A systematic review. *ISPRS J. Photogramm. Remote Sens.* **2021**, *171*, 330–347. [\[CrossRef\]](#)

26. Franch, B.; Cintas, J.; Becker-Reshef, I.; Sanchez-Torres, M.J.; Roger, J.; Skakun, S.; Sobrino, J.A.; Van Tricht, K.; Degerickx, J.; Whitcraft, A. Global crop calendars of maize and wheat in the framework of the WorldCereal project. *GIScience Remote Sens.* **2022**, *59*, 885–913. [[CrossRef](#)]
27. Cintas, J.; Franch, B.; Van-Tricht, K.; Boogaard, H.; Degerickx, J.; Becker-Reshef, I.; Moletto-Lobos, I.; Mollà-Bononad, B.; Sobrino, J.A.; Szantoi, Z. TRANCO: Thermo radiometric normalization of crop observations. *Int. J. Appl. Earth Obs. Geoinf.* **2023**, *118*, 103283. [[CrossRef](#)]
28. Girsang, S.S.; Stuart, A.M.; Parhusip, D.; Manurung, E.D.; Pabuayon, I.L.B.; Buresh, R.J. Mid-Season Adjustment of Nitrogen Fertilizer for Rice with Two Plant Spacings. *Field Crops Res.* **2023**, *302*, 109081. [[CrossRef](#)]
29. Shi, X.; Han, W.; Zhao, T.; Tang, J. Decision support system for variable rate irrigation based on UAV multispectral remote sensing. *Sensors* **2019**, *19*, 2880. [[CrossRef](#)]
30. Hunt, M.L.; Blackburn, G.A.; Carrasco, L.; Redhead, J.W.; Rowland, C.S. High resolution wheat yield mapping using Sentinel-2. *Remote Sens. Environ.* **2019**, *233*, 111410. [[CrossRef](#)]
31. Caballero, G.; Pezzola, A.; Winschel, C.; Casella, A.; Sanchez Angonova, P.; Orden, L.; Berger, K.; Verrelst, J.; Delegido, J. Quantifying Irrigated Winter Wheat LAI in Argentina Using Multiple Sentinel-1 Incidence Angles. *Remote Sens.* **2022**, *14*, 5867. [[CrossRef](#)]
32. Kalecinski, N.I.; Skakun, S.; Torbick, N.; Huang, X.; Franch, B.; Roger, J.C.; Vermote, E. Crop yield estimation at different growing stages using a synergy of SAR and optical remote sensing data. *Sci. Remote Sens.* **2024**, *10*, 100153. [[CrossRef](#)]
33. Jain, M.; Srivastava, A.K.; Joon, R.K.; McDonald, A.; Royal, K.; Lisaius, M.C.; Lobell, D.B. Mapping smallholder wheat yields and sowing dates using micro-satellite data. *Remote Sens.* **2016**, *8*, 860. [[CrossRef](#)]
34. Shevyrnogov, A.P.; Emelyanov, D.V.; Malchikov, N.O.; Demyanenko, T.N.; Ivchenko, V.K.; Botvich, I.Y. Early Forecasting of Crop Yields Based on PlanetScope Dove Satellite Data. *Biophysics* **2021**, *66*, 992–997. [[CrossRef](#)]
35. Holman, F.H.; Riche, A.B.; Michalski, A.; Castle, M.; Wooster, M.J.; Hawkesford, M.J. High throughput field phenotyping of wheat plant height and growth rate in field plot trials using UAV based remote sensing. *Remote Sens.* **2016**, *8*, 1031. [[CrossRef](#)]
36. Ganeva, D.; Roumenina, E.; Dimitrov, P.; Gikov, A.; Jeleu, G.; Dragov, R.; Bozhanova, V.; Taneva, K. Phenotypic traits estimation and preliminary yield assessment in different phenophases of wheat breeding experiment based on UAV multispectral images. *Remote Sens.* **2022**, *14*, 1019. [[CrossRef](#)]
37. Álvaro-Fuentes, J.; Cantero-Martínez, C.; López, M.V.; Arrúe, J.L. Soil carbon dioxide fluxes following tillage in semi-arid Mediterranean agroecosystems. *Soil Till. Res.* **2007**, *96*, 331–341. [[CrossRef](#)]
38. Soil Survey Staff. *Keys to Soil Taxonomy*, 13th ed.; USDA Natural Resources Conservation Service: Washington, DC, USA, 2022; p. 401.
39. Sánchez-Méndez, S.; Orden, L.; Mira-Urios, M.A.; Andreu-Rodríguez, J.; Saéz, J.A.; Martínez-Sabater, E.; Álvaro-Fuentes, J.; Moral, R. Validación Agronómica de nuevas estrategias de fertilización orgánicas y orgánico minerales en un cultivo de trigo. In Proceedings of the Book of Abstracts: 8ª Jornadas Red Española de Compostaje; Córdoba, España, 2–4 October 2024; ISBN 978-84-09-65478-9.
40. Zadoks, J.C.; Chang, T.T.; Konzak, C.F. A decimal code for the growth stages of cereals. *Weed Res.* **1974**, *14*, 415–421. [[CrossRef](#)]
41. Plaza-Bonilla, D.; Álvaro-Fuentes, J.; Hansen, N.C.; Lampurlanés, J.; Cantero-Martínez, C. Winter cereal root growth and aboveground–belowground biomass ratios as affected by site and tillage system in dryland Mediterranean conditions. *Plant Soil* **2014**, *374*, 925–939. [[CrossRef](#)]
42. García Rández, A.; Orden, L.; Marks, E.A.N.; Andreu-Rodríguez, F.J.; Franco-Luesma, S.; Martínez Sabater, E.; Saéz-Tovar, J.A.; Pérez-Murcia, M.D.; Agulló, E.; Bustamante, M.A. Monitoring of greenhouse gas emissions and compost quality during olive mill waste co-composting at industrial scale: The effect of N and C sources. *Waste Manag.* **2024**; *Accepted-Under Review*.
43. Patrignani, A.; Ochsner, T. Canopeo: A Powerful New Tool for Measuring Fractional Green Canopy Cover. *Agron. J.* **2015**, *107*, 2312–2320. [[CrossRef](#)]
44. Casella, A.; Orden, L.; Pezzola, N.A.; Bellacomo, C.; Winschel, C.I.; Caballero, G.R.; Delegido, J.; Gracia, L.M.N.; Verrelst, J. Analysis of Biophysical Variables in an Onion Crop (*Allium cepa* L.) with Nitrogen Fertilization by Sentinel-2 Observations. *Agronomy* **2022**, *12*, 1884. [[CrossRef](#)]
45. Kabata-Pendias, A. *Trace Elements in Soils and Plants*, 4th ed.; CRC Press: Boca Raton, FL, USA, 2010; p. 548.
46. Bustamante, M.Á.; Michelozzi, M.; Barra Caracciolo, A.; Grenni, P.; Verbokkem, J.; Geerdink, P.; Safi, C.; Nogues, I. Effects of Soil Fertilization on Terpenoids and Other Carbon-Based Secondary Metabolites in *Rosmarinus officinalis* Plants: A Comparative Study. *Plants* **2020**, *9*, 830. [[CrossRef](#)]
47. Wringley, C.; Batey, I. *Assessing Grain Quality*; Cauvain, S.P., Ed.; Food Science, Technology and Nutrition: Washington, DC, USA, 2003; pp. 71–96. [[CrossRef](#)]
48. Di Rienzo, J.A.; Casanoves, F.; Balzarini, M.G.; Gonzalez, L.; Tablada, M.; Robledo, C.W. InfoStat Versión. Centro de Transferencia InfoStat, FCA, Universidad Nacional de Córdoba, Argentina. 2020. Available online: <http://www.infostat.com.ar> (accessed on 6 June 2024).
49. Planet Understanding PlanetScope Instruments. Available online: <https://developers.planet.com/docs/apis/data/sensors/> (accessed on 4 July 2024).
50. Planet Labs. *PlanetScope Imagery Product Specification*; Planet Labs: San Francisco, CA, USA, 2023; pp. 1–39. Available online: https://assets.planet.com/docs/Planet_PSScene_Imagery_Product_Spec_letter_screen.pdf (accessed on 20 November 2024).

51. Vermote, E.F.; Tanré, D.; Deuze, J.L.; Herman, M.; Morcette, J.J. Second simulation of the satellite signal in the solar spectrum, 6S: An overview. *IEEE Trans. Geosci. Remote Sens.* **1997**, *35*, 675–686. [[CrossRef](#)]
52. Aqua Product Descriptions: MOD09CMA. MODIS/Terra Aerosol Optical Thickness Daily L3 Global 0.05Deg CMA [Data Set]. NASA. Published 12 February 2015. Available online: <https://modaps.modaps.eosdis.nasa.gov/services/about/products/c6-nrt/MOD09CMA.html> (accessed on 16 November 2024).
53. Vermote, E. MODIS/Terra Surface Reflectance Daily L3 Global 0.05Deg CMG V061 [Data set]; NASA EOSDIS Land Processes Distributed Active Archive Center. 2021. Available online: <https://lpdaac.usgs.gov/products/mod09cmgv061/> (accessed on 16 November 2024).
54. Platnick, S. MODIS Atmosphere L3 Daily Product; NASA MODIS Adaptive Processing System, Goddard Space Flight Center. USA, 2015. Available online: https://ladsweb.modaps.eosdis.nasa.gov/missions-and-measurements/products/MOD08_D3 (accessed on 16 November 2024).
55. Westoby, M.J.; Brasington, J.; Glasser, N.F.; Hambrey, M.J.; Reynolds, J.M. ‘Structure-from-Motion’ photogrammetry: A low-cost, effective tool for geoscience applications. *Geomorphology* **2012**, *179*, 300–314. [[CrossRef](#)]
56. Radiometric Calibration Model for MicaSense Sensors. Available online: <https://support.micasense.com/hc/en-us/articles/115000351194-Radiometric-Calibration-Model-for-MicaSense-Sensors> (accessed on 16 November 2024).
57. Use of Calibrated Reflectance Panels for MicaSense Data. Available online: <https://support.micasense.com/hc/en-us/articles/115000765514-Use-of-Calibrated-Reflectance-Panels-For-MicaSense-Data> (accessed on 16 November 2024).
58. QGIS Geographic Information System. QGIS Association. Available online: <http://www.qgis.org> (accessed on 24 June 2024).
59. Rouse, J.W.; Haas, R.H.; Schell, J.A.; Deering, D.W. Monitoring Vegetation Systems in the Great Plains with ERTS. In Proceedings of the Third ERTS Symposium, Washington, DC, USA, 10–14 December 1973; pp. 309–317.
60. Tucker, C.J. Red and photographic infrared linear combinations for monitoring vegetation. *Remote Sens. Environ.* **1979**, *8*, 127–150. [[CrossRef](#)]
61. Savitzky, A.; Golay, M.J. Smoothing and differentiation of data by simplified least squares procedures. *Anal. Chem.* **1964**, *36*, 1627–1639. [[CrossRef](#)]
62. McMaster, G.S.; Wilhelm, W.W. Growing degree-days: One equation, two interpretations. *Agric. For. Meteorol.* **1997**, *4*, 291–300. [[CrossRef](#)]
63. Franch, B.; Vermote, E.F.; Becker-Reshef, I.; Claverie, M.; Huang, J.; Zhang, J.; Justice, C.; Sobrino, J.A. Improving the timeliness of winter wheat production forecast in the United States of America, Ukraine and China using MODIS data and NCAR Growing Degree Day information. *Remote Sens. Environ.* **2015**, *161*, 131–148. [[CrossRef](#)]
64. Jordan, C.F. Deviation of leaf-area index from quality of light on the forest floor. *Ecology* **1969**, *50*, 663–666. [[CrossRef](#)]
65. Huete, A.R. A soil-adjusted vegetation index (SAVI). *Remote Sens. Environ.* **1988**, *25*, 295–309. [[CrossRef](#)]
66. Clevers, J.G.P.W. The application of a weighted infrared-red vegetation index for estimating leaf-area index by correcting for soil-moisture. *Remote Sens. Environ.* **1989**, *29*, 25–37. [[CrossRef](#)]
67. Gitelson, A.A.; Merzlyak, M.N. Spectral reflectance changes associated with autumn senescence of *Aesculus hippocastanum* L. and *Acer platanoides* L. leaves. Spectral features and relation to chlorophyll estimation. *J. Plant Physiol.* **1994**, *143*, 286–292. [[CrossRef](#)]
68. Daughtry, C.S.T.; Walthall, C.S.; Kim, M.S.; De Colstoun, E.B.; McMurtrey, J.E. Estimating Corn Leaf Chlorophyll Concentration from Leaf and Canopy Reflectance. *Remote Sens. Environ.* **2000**, *74*, 229–239. [[CrossRef](#)]
69. Huete, A.; Didan, K.; Miura, T.; Rodriguez, E.; Gao, X.; Ferreira, L.G. Overview of the Radiometric and Biophysical Performance of the MODIS Vegetation Indices. *Remote Sens. Environ.* **2002**, *83*, 195–213. [[CrossRef](#)]
70. Vincini, M.; Frazzi, E.; D’Alessio, P. Comparison of narrow-band and broad-band vegetation indices for canopy chlorophyll density estimation in sugar beet. In Proceedings of the 6th European Conference on Precision Agriculture, Skiathos, Greece, 3–6 June 2007; pp. 189–196.
71. Delegido, J.; Verrelst, J.; Meza, C.M.; Rivera, J.P.; Alonso, L.; Moreno, J. A red-edge spectral index for remote sensing estimation of Green LAI over agroecosystems. *Eur. J. Agron.* **2013**, *46*, 42–52. [[CrossRef](#)]
72. Pasqualotto, N.; D’Urso, G.; Bolognesi, S.F.; Belfiore, O.R.; Van Wittenberghe, S.; Delegido, J.; Pezzola, A.; Winschel, C.; Moreno, J. Retrieval of Evapotranspiration from Sentinel-2: Comparison of Vegetation Indices, Semi-Empirical Models and SNAP Biophysical Processor Approach. *Agronomy* **2019**, *9*, 663. [[CrossRef](#)]
73. Silva AG, P.; Galvão, L.S.; Ferreira Júnior, L.G.; Teles, N.M.; Mesquita, V.V.; Haddad, I. Discrimination of Degraded Pastures in the Brazilian Cerrado Using the PlanetScope SuperDove Satellite Constellation. *Remote Sens.* **2024**, *16*, 2256. [[CrossRef](#)]
74. Skakun, S.; Franch, B.; Vermote, E.; Roger, J.C.; Becker-Reshef, I.; Justice, C.; Kussul, N. Early season large-area winter crop mapping using MODIS NDVI data, growing degree days information and a Gaussian mixture model. *Remote Sens. Environ.* **2017**, *195*, 244–258. [[CrossRef](#)]
75. Li, Z.; Zhao, Y.; Taylor, J.; Gaulton, R.; Jin, X.; Song, X.; Li, Z.; Meng, Y.; Chen, P.; Yang, G. Comparison and transferability of thermal, temporal and phenological-based in-season predictions of above-ground biomass in wheat crops from proximal crop reflectance data. *Remote Sens. Environ.* **2022**, *273*, 112967. [[CrossRef](#)]
76. Grigorieva, E.; Matzarakis, A.; Karmalkar, A. Effects of climatic and cultivar changes on winter wheat phenology in central Lithuania. *Int. J. Biometeorol.* **2022**, *66*, 2213–2228. [[CrossRef](#)]
77. Cottrell, B.; Kalacska, M.; Arroyo-Mora, J.P.; Lucanus, O.; Inamdar, D.; Løke, T.; Soffer, R.J. Limitations of a Multispectral UAV Sensor for Satellite Validation and Mapping Complex Vegetation. *Remote Sens.* **2024**, *16*, 2463. [[CrossRef](#)]

78. Jiang, L.; Yuan, C.; Li, Z.; Su, J.; Yi, Z.; Yao, W.; Wu, P.; Liu, Z.; Cheng, S.; Pan, M. Multi-band and high-sensitivity perfect absorber based on monolayer graphene metamaterial. *Diam. Relat. Mater.* **2021**, *111*, 108227. [[CrossRef](#)]
79. Leach, N.; Coops, N.C.; Obrknezev, N. Normalization method for multi-sensor high spatial and temporal resolution satellite imagery with radiometric inconsistencies. *Comput. Electron. Agric.* **2019**, *164*, 104893. [[CrossRef](#)]
80. Roy, D.P.; Huang, H.; Houborg, R.; Martins, V.S. A global analysis of the temporal availability of PlanetScope high spatial resolution multi-spectral imagery. *Remote Sens. Environ.* **2021**, *264*, 112586. [[CrossRef](#)]
81. Dong, M.; Liu, S.; Jiang, R.; Qi, J.; de Solan, B.; Comar, A.; Li, L.; Li, W.; Ding, Y.; Baret, F. Comparing and combining data-driven and model-driven approaches to monitor wheat green area index with high spatio-temporal resolution satellites. *Remote Sens. Environ.* **2024**, *305*, 114118. [[CrossRef](#)]
82. Kington, J.; Collison, A. *Scene Level Normalization and Harmonization of Planet Dove Imagery*; Planet Labs Inc.: San Francisco, CA, USA, 2022.
83. Li, C.; Wang, H.; Gao, Y.; Wang, X. Effects of Post-Anthesis Irrigation on the Activity of Starch Synthesis-Related Enzymes and Wheat Grain Quality under Different Nitrogen Conditions. *Plants* **2023**, *12*, 4086. [[CrossRef](#)] [[PubMed](#)]
84. Hou, P.; Gao, Q.; Xie, R.; Li, S.; Meng, Q.; Kirkby, E.A.; Römheld, V.; Müller, T.; Zhang, F.; Chen, X. Grain yields in relation to N requirement: Optimizing nitrogen management for spring maize grown in China. *Plant Soil* **2012**, *360*, 63–77. [[CrossRef](#)]

Disclaimer/Publisher's Note: The statements, opinions and data contained in all publications are solely those of the individual author(s) and contributor(s) and not of MDPI and/or the editor(s). MDPI and/or the editor(s) disclaim responsibility for any injury to people or property resulting from any ideas, methods, instructions or products referred to in the content.